



## Cite as

Nano-Micro Lett.  
(2025) 17:244Received: 21 January 2025  
Accepted: 4 March 2025  
© The Author(s) 2025

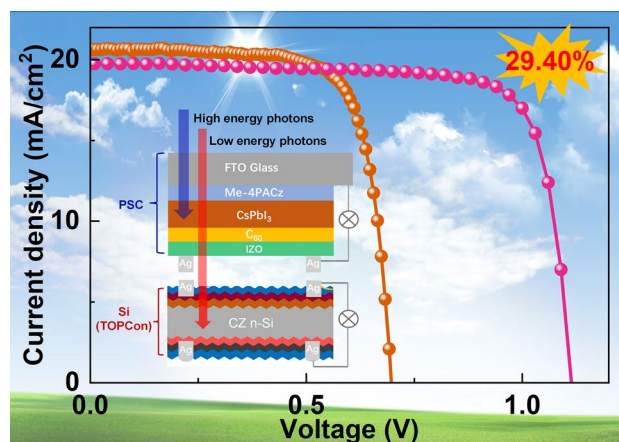
# Buried Interface Regulation with $\text{TbCl}_3$ for Highly-Efficient All-Inorganic Perovskite/Silicon Tandem Solar Cells

Wenming Chai<sup>1</sup>, Weidong Zhu<sup>1</sup> ✉, He Xi<sup>1,3</sup>, Dazheng Chen<sup>1</sup>, Hang Dong<sup>1</sup>, Long Zhou<sup>1</sup>, Hailong You<sup>1</sup>, Jincheng Zhang<sup>1</sup>, Chunfu Zhang<sup>1</sup> ✉, Chunxiang Zhu<sup>2</sup>, Yue Hao<sup>1</sup>

## HIGHLIGHTS

- The lanthanide compound of  $\text{TbCl}_3$  improved the wettability of Me-4PACz and further enhanced crystallization, in which the additional  $\text{Cl}^-$  ions passivate iodine vacancy and improve energy level alignment at buried interface.
- The inverted  $\text{CsPbI}_3$  PSCs with  $\text{TbCl}_3$  achieved a remarkable efficiency of 18.68% and enhanced stability in ambient air.
- Efficiencies of 29.40% and 25.44% were, respectively, achieved in 4T and 2T all-inorganic perovskite/silicon mechanically tandem devices.

**ABSTRACT** All-inorganic perovskite materials exhibit exceptional thermal stability and promising candidates for tandem devices, while their application is still in the initial stage. Here, a metal halide doping strategy was implemented to enhance device performance and stability for inverted  $\text{CsPbI}_3$  perovskite solar cells (PSCs), which are ideal for integration into perovskite/silicon tandem solar cells. The lanthanide compound terbium chloride ( $\text{TbCl}_3$ ) was employed to improve buried interface between [4-(3,6-Dimethyl-9H-carbazol-9-yl) butyl] phosphonic acid (Me-4PACz) and perovskite layer, thereby enhancing the crystallinity of  $\text{CsPbI}_3$  films and passivating non-radiative recombination defects. Thus, the inverted  $\text{CsPbI}_3$  PSCs achieved an efficiency of 18.68% and demonstrated excellent stability against water and oxygen. Meanwhile, remarkable efficiencies of 29.40% and 25.44% were, respectively, achieved in four-terminal (4T) and two-terminal (2T) perovskite/silicon mechanically tandem devices, which are higher efficiencies among reported all-inorganic perovskite-based tandem solar cells. This study presents a novel approach for fabricating highly efficient and stable inverted all-inorganic PSCs and perovskite/silicon tandem solar cells.



**KEYWORDS** All-inorganic perovskite; Tandem solar cells; Interface regulation; Chloride passivation

✉ Weidong Zhu, wdzhu@xidian.edu.cn; Chunfu Zhang, cfzhang@xidian.edu.cn

<sup>1</sup> State Key Laboratory of Wide-Bandgap Semiconductor Devices and Integrated Technology, School of Microelectronics, Xidian University, Xi'an 710071, People's Republic of China<sup>2</sup> Department of Electrical and Computer Engineering, National University of Singapore, 10 Kent Ridge Crescent, Singapore 119260, Singapore<sup>3</sup> Department of Nanomaterials, University of Melbourne, Parkville, Victoria 3010, Australia

## 1 Introduction

All-inorganic  $\text{CsPbI}_{3-x}\text{Br}_x$  ( $0 \leq x \leq 3$ ) perovskites demonstrate exceptional thermal stability ( $> 300^\circ\text{C}$ ) and possess an adjustable optical bandgap ranging from 1.7 to 2.3 eV, offering significant potential for integration into tandem devices with silicon and organic solar cells [1–5]. The efficiency of single-junction  $\text{CsPbI}_{3-x}\text{Br}_x$  perovskite solar cells (PSCs) has rapidly surpassed 22% [6–9]. However, the commonly used hole transport layer (HTL) of 2,2',7,7'-tetrakis [N,N-di(4-methoxyphenyl)amino]-9,9'-spirobifluorene (spiro-OMeTAD) exhibits high parasitic absorption, which hinders its application in tandem devices. Additionally, the 4-tert-butylpyridine (t-BP) and Li-bis(trifluoromethanesulfonyl) imide (Li-TFSI) dopants could absorb moisture from the air, negatively impacting device stability [10–12]. Compared to the conventional structure, the electron transport layer (ETL) of inverted structure can protect the perovskite layer, exhibiting superior moisture stability and reduced hysteresis effects [13, 14]. Consequently, inverted PSCs have become a focal point of research in the photovoltaic field.

Inverted all-inorganic PSCs primarily utilize  $\text{CsPbI}_3$  and  $\text{CsPbI}_2\text{Br}$  perovskite materials. Snaith et al. [15] first reported inverted  $\text{CsPbI}_3$  PSCs with an efficiency of 1.7%, which has since rapidly increased to achieve a record efficiency of 20.6% [16]. Compared to conventional structures, inverted all-inorganic PSCs exhibit inferior photovoltaic performance and larger open-circuit voltage ( $V_{\text{OC}}$ ) losses due to mismatched energy level alignment. Among common hole transport materials (HTMs), the hydrophilicity and acidity of PEDOT reduce interface stability, consequently decreasing the  $V_{\text{OC}}$  [17–19]. The wettability of precursor on the surfaces of poly[bis(4-phenyl) (2,4,6-trimethylphenyl) amine] (PTAA) is low, deteriorating the growth of perovskite films. The high annealing temperature restricts the application of organic HTLs in all-inorganic PSCs [20]. And, nickel oxide ( $\text{NiO}_x$ ) possesses low conductivity and high surface defects ( $\text{Ni}^{3+}$ ), which could hinder hole transfer, increase non-radiative recombination and accelerate perovskite degradation [14, 21]. Moreover, there is a detrimental reaction between  $\text{NiO}_x$  and dimethylammonium iodide (DMAI) in  $\text{CsPbI}_3$ , which adversely affects device performance [22]. The energy mismatch between the all-inorganic perovskite film and the HTL/ETL also results in lower efficiency of inverted devices

[19]. Tremendous efforts have been dedicated to optimizing the interface between perovskite and charge transport layers for synchronously enhanced PCE and stability of PSCs, such as bilayer homojunctions, ion-modulated radical doping [10–12, 23, 24]. Therefore, excellent charge transport materials can improve the crystallization of perovskite films and facilitate charge extraction at interfaces.

Ultra-thin self-assembled monolayers (SAMs) based on carbonyl units exhibit rich electron and high hole extraction capabilities, including [2-(3,6-dimethoxy-9H-carbazol-9-yl) ethyl] phosphonic acid (MeO-2PACz) and [4-(3,6-dimethyl-9H-carbazol-9-yl) butyl] phosphonic acid (Me-4PACz). The symmetric structure of carbonyl units results in a small dipole moment and enhanced charge transporting characteristics, as well as adjusts the work function of substrate [25, 26]. Currently, SAMs materials were commonly adopted to modify the interface between perovskite films and HTLs [22, 27–29]. Compared to other materials, Me-4PACz-based device exhibited the lower interface defects density ( $2 \times 10^9 \text{ cm}^{-2}$ ) and one of highest efficiencies for single-junction and tandem solar cells [30]. However, the carbonyl units may also cause steric hindrance and wetting issues, which are detrimental to the density, uniformity, and crystallinity of perovskite films [31–33]. Therefore, optimizing the wettability of SAM layers can improve the crystallization of perovskite films and enhance the performance of inverted all-inorganic PSCs.

In this work, we utilized Me-4PACz with high charge carrier mobility, low affinity, and good photostability to fabricate inverted all-inorganic  $\text{CsPbI}_3$  PSCs. Terbium chloride ( $\text{TbCl}_3$ ) doping was employed to improve buried interface between Me-4PACz and perovskite, resulting in larger grains, smooth surface and enhanced phase stability of  $\text{CsPbI}_3$  films. Meanwhile, chloride passivation reduced defect density and suppressed non-radiative recombination at the buried interface. This also improved the energy alignment between the  $\text{CsPbI}_3$  film and Me-4PACz, thereby increasing the efficiency of inverted  $\text{CsPbI}_3$  PSCs to 18.68%. Additionally, the four-terminal (4T) and two-terminal (2T) perovskite/silicon mechanically tandem devices achieved the efficiencies of 29.40% and 25.44%, respectively. This provides a novel method for preparing efficient and stable all-inorganic  $\text{CsPbI}_{3-x}\text{Br}_x$  PSCs and perovskite/silicon tandem devices, promoting the commercialization of perovskite photovoltaic technology.

## 2 Experimental Section

### 2.1 Materials and Reagents

Cesium iodide (CsI, 99.5%) and lead iodide (PbI<sub>2</sub>, 99.5%) were purchased from Alfa Aesar. Terbium trichloride (TbCl<sub>3</sub>, 99.5%), N,N-dimethylformamide (DMF, ≥ 99.9%), Dimethyl sulfoxide (DMSO, ≥ 99.9%), isopropyl alcohol (IPA, ≥ 99.9%), and chlorobenzene (CB, ≥ 99.9%) were purchased from Sigma-Aldrich. Dimethylammonium iodide (DMAI), Methylamine chloride (MACl), bathocuproine (BCP), C60, and (4-(3,6-dimethyl-9H-carbazole-9-yl)butyl) phosphonic acid (Me-4PACz, ≥ 99.9%) were purchased from Xi'an Yuri Solar Co., Ltd. All the above chemicals were used as received without any further purification.

### 2.2 Solution Preparation

The 0.7 M CsPbI<sub>3</sub> precursor was prepared by dissolving CsI, PbI<sub>2</sub> and DMAI with the 1:1:1 molar ratio in the mixed solvent of DMF and DMSO (9:1). Then, the 1 mg mL<sup>-1</sup> Me-4PACz and TbCl<sub>3</sub> were mixed in ethyl alcohol. All solutions were stirred with magnetic stirrers for 12 h.

### 2.3 Fabrication of CsPbI<sub>3</sub> Single-Junction Devices

The FTO/glass substrates were ultrasonically cleaned sequentially with Decon90, deionized water, acetone, and ethanol for 15 min, respectively. The FTO/glass substrates were dried with N<sub>2</sub> and treated with Ozone for 30 min. A Me-4PACz and TbCl<sub>3</sub> mixed solvent was spin-coated on FTO at 5000 rpm for 30 s, followed by annealing for 10 min at 100 °C. The 80 μL CsPbI<sub>3</sub> precursor was deposited on the Me-4PACz by spin-coating at 3000 rpm for 30 s. And, the CsPbI<sub>3</sub> films were obtained by annealing at 200 °C for 5 min. Subsequently, 20 nm C60 and 7 nm BCP were sequentially deposited by vacuum evaporation under a vacuum pressure of 5 × 10<sup>-4</sup> Pa. Finally, 100 nm silver (Ag) electrode was deposited with an active area of 0.07 cm<sup>2</sup> by vacuum evaporation to obtain the inverted structure CsPbI<sub>3</sub> PSCs.

### 2.4 Fabrication of 2T Mechanically Tandem Devices

First, an 80 nm indium zinc oxide (IZO) was deposited on the surface of C60 using radio frequency (RF) magnetron sputtering, serving as a semi-transparent electrode. Next, 100 nm Ag grid electrode was thermally evaporated to enhance conductivity, forming semi-transparent PSCs. Finally, the prepared semi-transparent PSCs were affixed onto silicon solar cells and secured along the edges with high-temperature adhesive tape, completing the perovskite/silicon 2T mechanically stacked solar cell.

### 2.5 Characterizations

SEM images were obtained by a Helios NanoLab G3 SEM. XPS and UPS spectra were acquired from X-ray photoelectron spectroscopy (Nexsa, Thermo Fisher). XRD was measured by an x'pert3 powder X-ray diffractometer (PANalytical, Netherlands). UV-vis absorption spectra were obtained by a spectrophotometer (U-4100, Hitachi). Steady-state PL and TRPL were tested on a FluoTime 300 spectrometer (PicoQuant, German). Light J-V curves were recorded from 1.3 to -0.2 V with a step of 0.03 V s<sup>-1</sup> by a Keithley 2450 source meter under a simulated AM 1.5G illumination (100 mW cm<sup>-2</sup>), which was produced by an Oriel 92251A-1000 sunlight simulator. EQE was carried out on a 150 W xenon lamp (Oriel) equipped with a monochromator (Cornerstone 74,004). Dark I-V curves were obtained by Keithley 2636 source meter. EIS and Mott-Schottky were tested on an electrochemical workstation (CHI 660B) under dark conditions. The 1 V forward bias was applied to the EIS measurements. TPC and TPV were recorded by an oscilloscope, in which the sampling resistor of 50 Ω or 1 MΩ was applied. The photocurrent decay was measured under a 532 nm pulse laser (1000 Hz, 3.2 ns). The photovoltage decay was carried out under a 405 nm pulse laser (50 Hz, 20 ms). Contact angle was measured by OCA15EC with a precursor droplet of 5 μL.



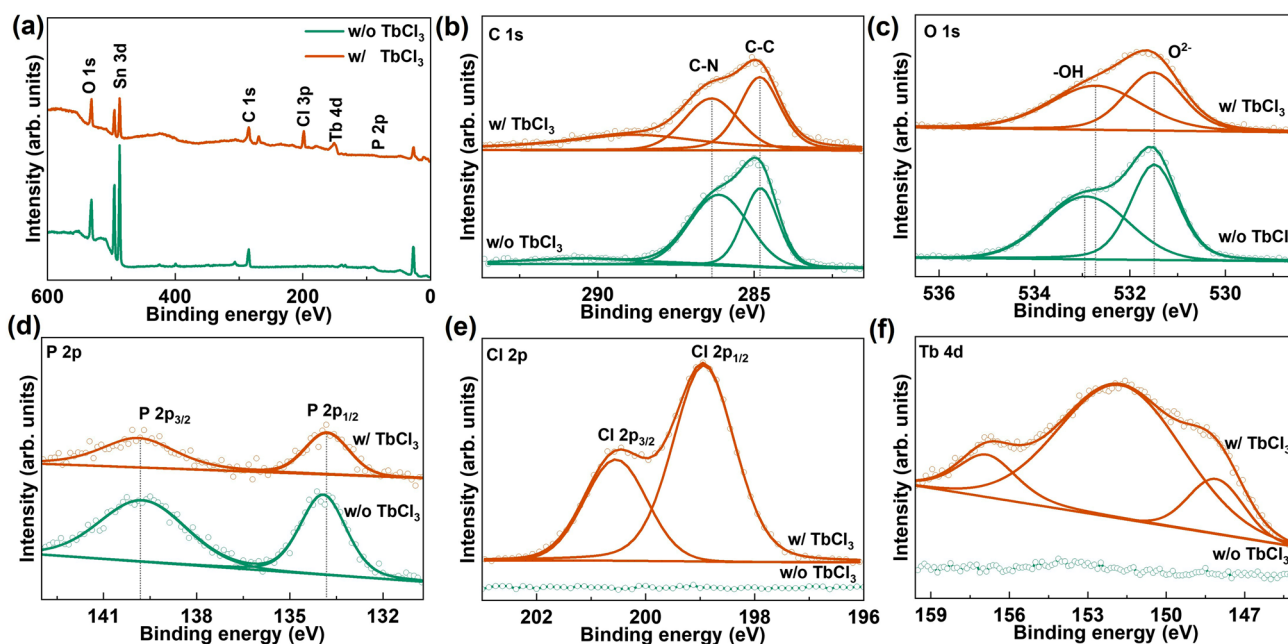


**Fig. 1** Surface chemistry of perovskite films. **a** XPS survey spectrum, **b** C 1s, **c** O 1s, **d** P 2p, **e** Cl 2p, and **f** Tb 4d core-level XPS spectra of the FTO/Me-4PACz substrate with and without TbCl<sub>3</sub> doping

### 3 Results and Discussion

#### 3.1 Surface Chemistry of Perovskite Films with Buried Interface Regulation

Me-4PACz is commonly used as an HTL to improve efficiency in both single-junction and perovskite/silicon tandem solar cells. Lanthanide ions (Ln<sup>3+</sup>) are employed to eliminate deep-level defects between the perovskite and HTL, thereby enhancing film quality [34, 35]. The doping state of TbCl<sub>3</sub> in Me-4PACz was characterized using X-ray photoelectron spectroscopy (XPS). Then, XPS spectra were calibrated with the C 1s peak (284.8 eV). As shown in Fig. 1, the C 1s, O 1s, and P 2p spectra indicate that the Me-4PACz was successfully adhesion to the FTO substrate, while the Cl 2p and Tb 4d spectra confirm the incorporation of TbCl<sub>3</sub> into Me-4PACz [36]. Compared to pure Me-4PACz on FTO, the OH- and P 2p XPS peaks shift toward higher binding energy in the sample with TbCl<sub>3</sub> doping, indicating that the electrical properties were changed. During the annealing process, doped ions tend to diffuse from the buried interface to surface, thereby affecting the optoelectronic properties of the perovskite film. To investigate the impact of TbCl<sub>3</sub> on the components, the surface composition of CsPbI<sub>3</sub> films was

characterized using XPS. As shown in Fig. S1, Tb 4d and Cl 2p were not detected in CsPbI<sub>3</sub> films based on TbCl<sub>3</sub>-doped Me-4PACz, indicating that Tb<sup>3+</sup> and Cl<sup>-</sup> did not diffuse to the surface. The Pb 4f and Cs 3d XPS peaks shifted to higher binding energy, whereas the I 3d shifted to lower binding energy. The difference in ionic radii leads to distortion in the BX<sub>6</sub> (B = Pb/Tb, X = I/Cl) octahedral structure, thus altering the surface chemical characteristics [28, 29]. These shifts are primarily attributed to the incorporation of Tb<sup>3+</sup> and Cl<sup>-</sup> into the CsPbI<sub>3</sub> crystal structure, where they, respectively, occupied Pb<sup>2+</sup> and I<sup>-</sup> sites. Additionally, excessive Cl<sup>-</sup> can passivate V<sub>I</sub> defects at buried interface, thereby enhancing the device optoelectronic properties.

#### 3.2 Improved Morphology and Crystal Quality of Buried Interface Regulation with TbCl<sub>3</sub>

The non-polar groups of long alkyl chains (C<sub>4</sub>H<sub>8</sub>) in Me-4PACz causes high hydrophobicity, resulting in poor coverage of the perovskite film. Metal ion have commonly been used to improve the wettability of the substrate [32, 37]. The effect of TbCl<sub>3</sub> on the wettability of Me-4PACz was performed using contact angle measurements. As shown

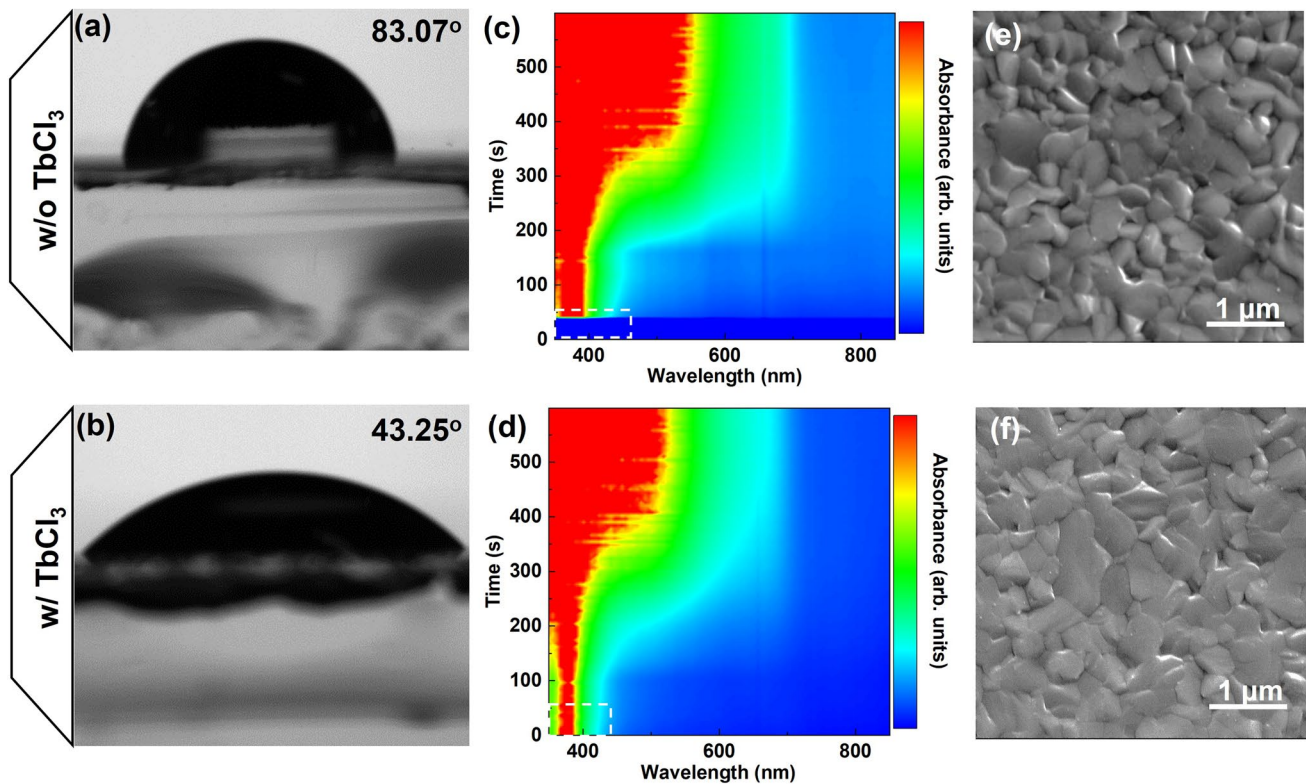


**Fig. 2** Crystallization process and Morphology of perovskite films. Contact angles of the CsPbI<sub>3</sub> precursor solution on the surface of Me-4PACz **a** without and **b** with TbCl<sub>3</sub> doping, respectively. In situ absorption spectra of CsPbI<sub>3</sub> intermediate phase films based on Me-4PACz **c** without and **d** with TbCl<sub>3</sub> doping during the annealing process, respectively. SEM images of CsPbI<sub>3</sub> films deposited on Me-4PACz **e** without and **f** with TbCl<sub>3</sub> doping

in Fig. 2a, b, TbCl<sub>3</sub> doping significantly reduced the contact angle of the CsPbI<sub>3</sub> precursor solution on substrate from 83.07° to 43.25°. Compared to Me-4PACz, the lower contact angle on TbCl<sub>3</sub>-doped Me-4PACz facilitates the spreading of the precursor solution, leading to fully covered and uniform perovskite film. This is contributed to enhance the crystallization and reduce surface roughness of the CsPbI<sub>3</sub> perovskite film. To investigate the influence of TbCl<sub>3</sub> doping on the crystallization process, in situ absorption spectroscopy was used to characterize the crystallization of CsPbI<sub>3</sub> films during the annealing process. As shown in Fig. 2c, d, the CsPbI<sub>3</sub> film without TbCl<sub>3</sub> doping shows no obvious absorption within the first 50 s, whereas the CsPbI<sub>3</sub> film based on TbCl<sub>3</sub>-doped Me-4PACz exhibits strong absorption in the short-wavelength region at the beginning. After approximately 250 s, the absorption edges of both films show no significant changes, indicating that TbCl<sub>3</sub> can accelerate the phase transition process of the CsPbI<sub>3</sub> film [38]. As shown in Fig. 2e, f, TbCl<sub>3</sub> doping

in Me-4PACz significantly enhances the crystallization quality in comparison with the control sample, resulting in CsPbI<sub>3</sub> films with larger grain sizes and uniform distribution. Moreover, the cross sectional SEM images are presented in Fig. S2, in which the control sample exhibits pinholes at interface between FTO and perovskite film. However, the CsPbI<sub>3</sub> film with TbCl<sub>3</sub> does not have obvious pinholes at interface due to the reduced contact angle of precursor on Me-4PACz, which is conducive to enhance the  $V_{OC}$  and short-circuit current density ( $J_{SC}$ ) of devices. And, the atomic force microscopy (AFM) images are shown in Fig. S3, the CsPbI<sub>3</sub> film with TbCl<sub>3</sub> doping has a lower root mean square (RMS) roughness of 19.0 nm in comparison with the control samples of 24.8 nm, similar to the SEM results. Therefore, TbCl<sub>3</sub> improves the wettability of Me-4PACz and accelerates the phase transition rate, forming CsPbI<sub>3</sub> films with great morphology. This can enhance the interface contact between the perovskite films and ETL, contributing to the improved optoelectronic performance.

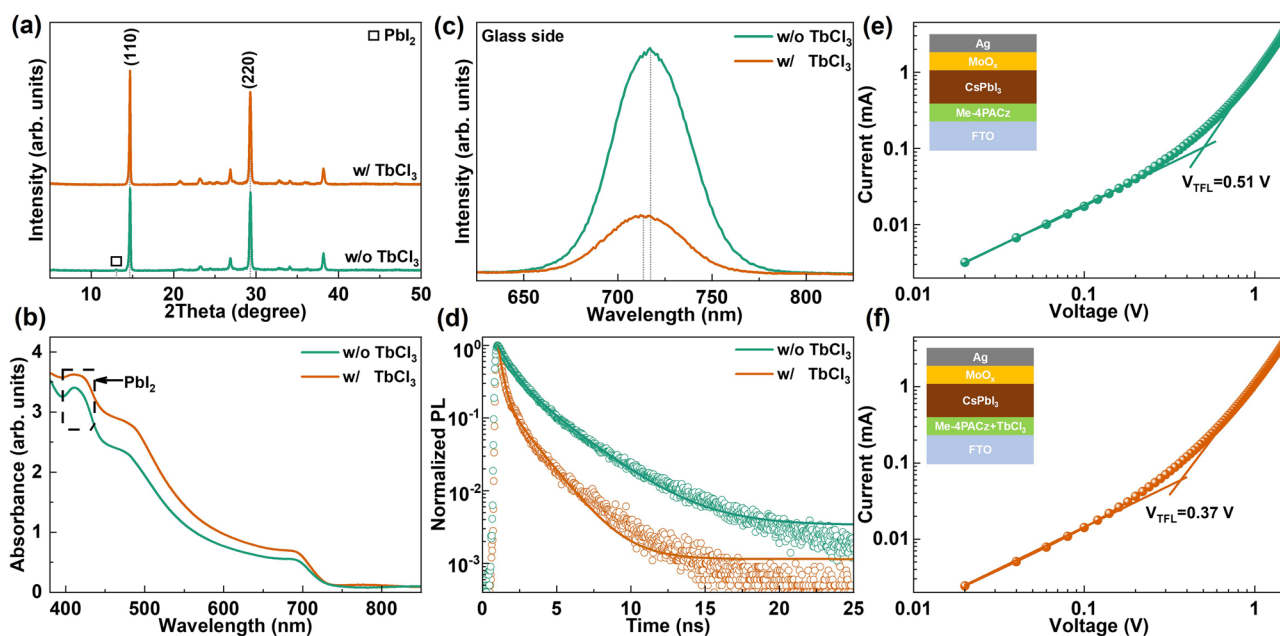


**Fig. 3** **a** XRD patterns, **b** UV–vis absorption spectra, **c** steady-state PL spectra, and **d** TRPL curves of CsPbI<sub>3</sub> films on Me-4PACz with and without TbCl<sub>3</sub> doping, respectively. **e**, **f** SCLC curves of CsPbI<sub>3</sub> films based on Me-4PACz without and with TbCl<sub>3</sub> doping

To further investigate the effect of TbCl<sub>3</sub> on the CsPbI<sub>3</sub> films, X-ray diffraction (XRD), ultraviolet–visible spectroscopy (UV–vis), photoluminescence (PL), time-resolution photoluminescence (TRPL), and space-charge-limited current (SCLC) were used to characterize the optoelectronic properties of the perovskite films. As shown in Fig. 3a, there are two diffraction peaks at 14.71° and 29.28°, corresponding to the (110) and (220) crystal planes of  $\gamma$ -CsPbI<sub>3</sub> [7–9]. Compared to the control sample, the CsPbI<sub>3</sub> film based on TbCl<sub>3</sub>-doped Me-4PACz exhibits stronger diffraction peaks, indicating that TbCl<sub>3</sub> significantly enhances the crystallinity of the perovskite film, which is consistent with the observed SEM results. The control sample shows a small XRD peak at 13.09°, corresponding to excessive PbI<sub>2</sub>. However, the CsPbI<sub>3</sub> film prepared with TbCl<sub>3</sub>-doped Me-4PACz does not exhibit PbI<sub>2</sub> peak, indicating that TbCl<sub>3</sub> suppresses the formation of excessive PbI<sub>2</sub> [39]. As presented in Fig. S4, the (110) and (220) peaks of the CsPbI<sub>3</sub> film prepared with TbCl<sub>3</sub>-doped Me-4PACz shift to smaller angles in comparison with the control sample. This indicates that the lattice constant was reduced according to Bragg’s law, proving that the smaller ionic radii of Tb<sup>3+</sup> and Cl<sup>-</sup> are incorporated into the CsPbI<sub>3</sub> lattice [28, 40, 41]. Ions doping leads to

chemical changes in CsPbI<sub>3</sub> film with TbCl<sub>3</sub>, as observed in XPS results. As shown in Fig. 3b, both samples have similar absorption onsets (~725 nm), corresponding to an optical bandgap of 1.71 eV. Similar to the XRD results, the CsPbI<sub>3</sub> film with TbCl<sub>3</sub> exhibits higher absorbance intensity, indicating that TbCl<sub>3</sub> enhances the crystallinity of the perovskite film. The control sample shows an exciton absorption peak at 410 nm, according to reported literature, which corresponds to excess PbI<sub>2</sub> components [42, 43]. Therefore, TbCl<sub>3</sub> doping in Me-4PACz significantly enhances the crystallinity of CsPbI<sub>3</sub> films and suppresses the formation of excess PbI<sub>2</sub>.

The interface property was performed using PL results obtained from the surface and glass substrate sides, respectively. As presented in Fig. S5, both samples exhibit similar PL peaks at 725 nm, consistent with the aforementioned absorption results. The CsPbI<sub>3</sub> film prepared with TbCl<sub>3</sub>-doped Me-4PACz shows higher PL intensity and blue shift in comparison with control sample, attributed to TbCl<sub>3</sub> enhancing the crystallinity of the CsPbI<sub>3</sub> film and reducing defect density. The PL results obtained from the glass substrate side were used to investigate the buried interface between the perovskite film and Me-4PACz. As shown in Fig. 3c, the CsPbI<sub>3</sub> film prepared

with  $\text{TbCl}_3$ -doped Me-4PACz exhibits a lower PL intensity and blue shift, indicating that  $\text{TbCl}_3$  incorporated into the lattice forms wide-bandgap perovskite and improves carrier extraction at the buried interface [44]. Similar results can be also derived from TRPL in Fig. 3d, the  $\text{CsPbI}_3$  film prepared with  $\text{TbCl}_3$ -doped Me-4PACz has a faster PL decay compared to the control sample. As displayed in Table S1, the fast decay part  $\tau_1$  decreases from 0.46 to 0.28 ns, and the slow decay part increases from 1.66 to 2.79 ns after  $\text{TbCl}_3$  modification. As a result, the average lifetime decreased from 2.67 to 1.55 ns after modifying with  $\text{TbCl}_3$ . Smaller  $\tau_1$  and larger  $\tau_2$  value indicate the rapid extraction of charge and the reduction of defect state density at the modified perovskite buried interface. Based on the SCLC theory, the defect densities of  $\text{CsPbI}_3$  films with and without  $\text{TbCl}_3$  were analyzed. Figure 3e, f shows the  $J$ - $V$  curves of single-hole devices, with the device structure illustrated in the inset. They display ohmic behavior at low bias, accompanied by a nonlinear increase in current density as the voltage exceeds trap-filled limit voltage ( $V_{\text{TFL}}$ ), which is directly proportional to the trap-state density ( $n_t$ ) according to the following equation [7]:

$$n_t = \frac{2V_{\text{TFL}}\epsilon_0\epsilon_r}{eL^2}$$

where the  $e$  is the elementary charge ( $e = 1.6 \times 10^{-19}$  C),  $\epsilon_0$  and  $\epsilon_r$  are vacuum permittivity ( $\epsilon_0 = 8.85 \times 10^{-12}$  F  $\text{m}^{-1}$ ) and relative permittivity ( $\epsilon_r = 6.32$ ),  $L$  is the thickness of perovskite film ( $L = 500$  nm), respectively [45, 46]. As indicated, the  $\text{CsPbI}_3$  films prepared with  $\text{TbCl}_3$ -doped Me-4PACz obtains a lower  $V_{\text{TFL}}$  of 0.37 V than the control device of 0.51 V, leading to a lower of  $1.035 \times 10^{15}$  vs.  $1.427 \times 10^{15}$   $\text{cm}^{-3}$ . Based on the above results,  $\text{TbCl}_3$  enhances the crystallinity and reduces defect density of  $\text{CsPbI}_3$  films, as well as improves carrier extraction capability at the buried interface, contributing to enhanced device performance.

### 3.3 Performance of Inverted $\text{CsPbI}_3$ Single-Junction Device

To investigate the effect of  $\text{TbCl}_3$  doping on the photovoltaic performance, we fabricated inverted  $\text{CsPbI}_3$  PSCs based on the device structure of FTO/Me-4PACz/ $\text{CsPbI}_3$ /C60/BCP/Cu. The surface work function and energy band alignment of Me-4PACz were measured using ultraviolet

photoelectron spectroscopy (UPS). As shown in Fig. S6,  $\text{TbCl}_3$  doping reduces the work function of Me-4PACz from 4.18 to 4.01 eV, with corresponding  $E_{\text{VBM}}$  values of  $-5.01$  and  $-5.07$  eV, respectively. Using the reported energy band values of other materials, the energy band alignment of  $\text{CsPbI}_3$  PSCs was obtained [47]. As shown in Fig. 4a,  $\text{TbCl}_3$  reduces the VBM difference between  $\text{CsPbI}_3$  films and Me-4PACz, facilitating hole extraction and transport, thereby improving the  $V_{\text{OC}}$  and PCE of the device [44, 48–50]. Figure 4b shows the current density–voltage ( $J$ - $V$ ) curves of devices with different amounts of  $\text{TbCl}_3$  dopants, and the photovoltaic parameters are statistically distributed in Fig. S7, in which the optimal concentration is  $1 \text{ mg mL}^{-1}$  and used in other characterizations. As shown in Fig. 4c and Table S2, the control sample exhibits a maximum PCE of 15.34%, with a  $V_{\text{OC}}$  of 1.017 V, fill-factor (FF) of 0.758, and  $J_{\text{SC}}$  of  $19.90 \text{ mA cm}^{-2}$ . For the  $\text{CsPbI}_3$  PSCs prepared with  $\text{TbCl}_3$ -doped Me-4PACz, the PCE increases to 18.68%, with a  $V_{\text{OC}}$  of 1.162 V and FF of 0.799. As the  $J$ - $V$  curves of the  $\text{CsPbI}_3$  PSC under forward and reverse scan are shown in Fig. S8, the device fabricated with  $\text{TbCl}_3$ -doped Me-4PACz generates less hysteresis. Due to the improved crystallization, the  $\text{CsPbI}_3$  film fabricated with  $\text{TbCl}_3$ -doped Me-4PACz exhibits few ions migration and non-radiative recombination near interfaces. Moreover, the  $\text{TbCl}_3$  doping decreases dark current of  $\text{CsPbI}_3$  PSCs, as provided in Fig. S9, which revealed that the leakage channel is suppressed to reduce the non-radiative recombination. The remarkable enhancement in these photovoltaic performance parameters should be ascribed to the improved optoelectronic properties of  $\text{CsPbI}_3$  film based on Me-4PACz with  $\text{TbCl}_3$ .

The photovoltaic parameters of 20 independent devices were statistically analyzed, as presented in Figs. 4d and S10. Compared to the control sample, the  $\text{CsPbI}_3$  PSCs prepared with  $\text{TbCl}_3$ -doped Me-4PACz exhibit higher average  $V_{\text{OC}}$ , FF and PCE values. This is consistent with the trend observed in the  $J$ - $V$  results, indicating that the  $\text{TbCl}_3$ -doped Me-4PACz method has good reproducibility. Figure 4e shows the EQE spectra of the  $\text{CsPbI}_3$  PSCs with a photo-response cut-off edge at  $\sim 725$  nm, which is consistent with the absorption results. The integrated current is  $18.60 \text{ mA cm}^{-2}$ , closing to the  $J_{\text{SC}}$  value of the device. Moreover, the steady-state output current density at the maximum power point was employed to evaluate the operational stability, as shown in Fig. 4f. Compared to the control sample, the  $\text{CsPbI}_3$  PSC

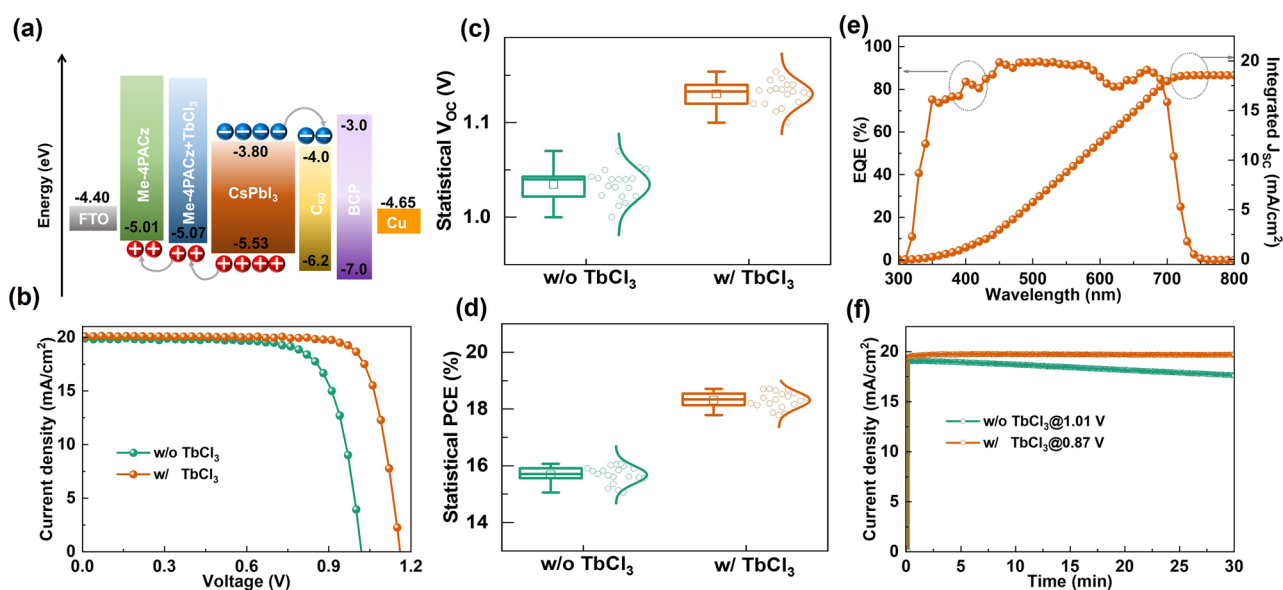


**Fig. 4** Influence of  $\text{TbCl}_3$  on PSCs performance. **a** Energy band alignment diagram of  $\text{CsPbI}_3$  PSCs based on Me-4PACz with and without  $\text{TbCl}_3$  doping. **b**  $J$ - $V$  curves of the  $\text{CsPbI}_3$  PSCs with varying  $\text{TbCl}_3$  concentrations. **c** Light  $J$ - $V$  curves and **d** Statistical PCE of  $\text{CsPbI}_3$  PSCs based on Me-4PACz with and without  $\text{TbCl}_3$  doping, respectively. **e** EQE spectra and integrated current curves of  $\text{CsPbI}_3$  PSCs based on Me-4PACz. **f** Steady-state output curves at the maximum power point of  $\text{CsPbI}_3$  PSCs based on Me-4PACz with and without  $\text{TbCl}_3$  doping

prepared with  $\text{TbCl}_3$ -doped Me-4PACz maintains a constant photocurrent density after 30 min under continuous illumination. In situ absorption spectroscopy was used to perform the effect of  $\text{TbCl}_3$  on the stability of  $\text{CsPbI}_3$  films in ambient air. As shown in Fig. 5, the absorption onset of the control sample gradually blue-shifts, while that of the  $\text{CsPbI}_3$  film prepared with  $\text{TbCl}_3$ -doped Me-4PACz remains almost unchanged after 1000 s. This indicates that  $\text{TbCl}_3$  significantly enhances the water and oxygen stability of the perovskite film [41, 51]. Moreover, as depicted in Fig. 5c, d, we measured the XRD patterns of unencapsulated  $\text{CsPbI}_3$  films after storing in ambient air. The intensity of control  $\text{CsPbI}_3$  films is reduced after storing for 5 days, and forming an additional peak at  $10.2^\circ$  corresponding to the  $\delta$ -phase. In comparison, the  $\text{CsPbI}_3$  films prepared with  $\text{TbCl}_3$ -doped Me-4PACz does not decrease the intensity and form additional peaks. Furthermore, the PL intensity of  $\text{CsPbI}_3$  films without  $\text{TbCl}_3$  is reduced after storing for 5 days, as shown in Fig. S11, whereas it does not change in the  $\text{CsPbI}_3$  films prepared with  $\text{TbCl}_3$ -doped Me-4PACz. The  $\delta$ -phase can result in enhanced non-radiative recombination, thereby reduce  $V_{\text{OC}}$  and PCE over time, as shown in Fig. S12. Overall,  $\text{TbCl}_3$  passivates interfacial defects and improves energy

band alignment, meanwhile enhancing the photovoltaic performance and stability of  $\text{CsPbI}_3$  PSCs.

Carrier dynamics of  $\text{CsPbI}_3$  PSCs were thoroughly investigated using transient photocurrent (TPC)/transient photovoltage (TPV), electrochemical impedance spectroscopy (EIS), and Mott-Schottky (M-S) characterizations. Figure S13a, b displays the TPC and TPV curves, fitted with a single exponential decay function. The  $\text{CsPbI}_3$  PSCs prepared with  $\text{TbCl}_3$ -doped Me-4PACz exhibit faster photocurrent decay ( $\tau_{\text{ave}} = 0.59 \mu\text{s}$ ) and slower photovoltage decay ( $\tau_{\text{ave}} = 0.031 \text{ ms}$ ), indicating that  $\text{TbCl}_3$  enhances carrier extraction and reduces carrier recombination [52, 53]. This also well support the results of PL and TRPL. As shown in Fig. S14a,  $\text{CsPbI}_3$  PSCs prepared with  $\text{TbCl}_3$ -doped Me-4PACz improved recombination resistance ( $R_{\text{rec}}$ ) from 2069 to 3198  $\Omega$  in comparison with the control sample, indicating that the carrier recombination is suppressed at the Me-4PACz/ $\text{CsPbI}_3$  interface [29, 54]. From the  $M$ - $S$  plot in Fig. S14b, the built-in voltage ( $V_{\text{bi}}$ ) values for  $\text{CsPbI}_3$  PSCs without and with  $\text{TbCl}_3$  doping were fitted to be 1.05 and 1.19 V, respectively. A relatively larger  $V_{\text{bi}}$  implies stronger driving force for carrier transport and wider depletion region to reduce carrier

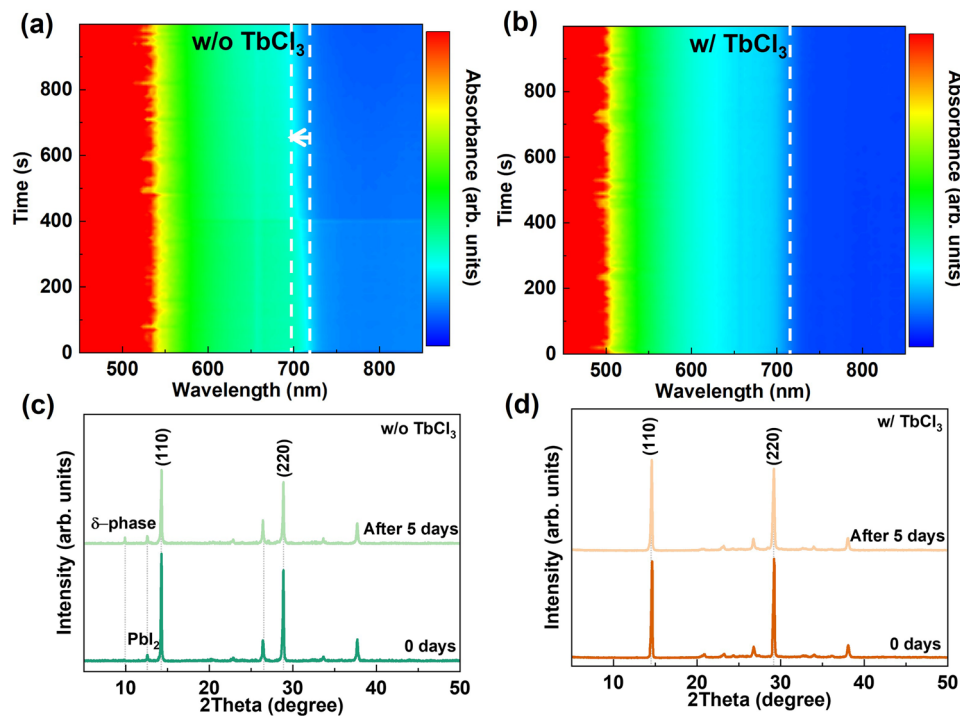


**Fig. 5** In situ absorption spectra of CsPbI<sub>3</sub> films prepared on Me-4PACz **a** without and **b** with TbCl<sub>3</sub> doping in air environment, respectively. XRD patterns of CsPbI<sub>3</sub> films prepared **c** without and **d** with TbCl<sub>3</sub>-doped Me-4PACz after storing for 5 days in ambient air

recombination, which is contributed to improve the  $V_{OC}$  of CsPbI<sub>3</sub> PSCs as JV results [44, 55]. Ultimately, the performance improvement of CsPbI<sub>3</sub> PSCs is attributed to the beneficial characteristics of CsPbI<sub>3</sub> films prepared with TbCl<sub>3</sub>-doped Me-4PACz, including larger grain size, high crystallinity, low defect density, and improved energy band alignment.

### 3.4 Performance of All-Inorganic Perovskite/Silicon Tandem Device

There are two basic structures for perovskite/silicon tandem solar cells. The 4T tandem structure has no specific requirements for the bandgap of the top cell, and the 2T tandem structure requires the top cell with bandgap of  $\sim 1.7$  eV. Therefore, wide-bandgap inverted CsPbI<sub>3</sub> PSCs are suitable as the top cell in tandem devices [56, 57]. As shown in Fig. 6a, semi-transparent CsPbI<sub>3</sub> PSCs were fabricated using IZO as the transparent electrode. As shown in Fig. 6c and Table S3, the optimal efficiency of semi-transparent inverted CsPbI<sub>3</sub> PSCs is 17.57%. Compared to the metal electrode,  $V_{OC}$  of semi-transparent device is reduced because of the damage to C60 during

the IZO sputtering process. The small-area ( $2 \times 2.5$  cm<sup>2</sup>) silicon solar cell has an efficiency of 11.83% after shading with the semi-transparent CsPbI<sub>3</sub> PSCs. Therefore, the 4T all-inorganic CsPbI<sub>3</sub> perovskite/silicon tandem solar cells obtained a remarkable PCE of 29.40% by simply adding the efficiencies of two sub-cells. Moreover, as presented in Fig. 6b, a mechanically stacked 2T perovskite/silicon tandem solar cell was fabricated using MXene with high transmittance and conductivity as the interconnection layer, referenced to our previous work [58, 59]. As shown in Fig. 6d, the 2T mechanically tandem devices achieved an optimal efficiency of 25.44% with  $V_{OC}$  of 1.75 V, FF of 0.783, and  $J_{SC}$  of 18.56 mA cm<sup>-2</sup>, which is one of high efficiencies of all-inorganic perovskite tandem solar cells. The photovoltaic parameters of the previously reported perovskite/silicon tandem solar cells based on inorganic perovskite are summarized in Table S4 and the results of the corresponding PCE distributions are shown in Fig. 6e. As shown in Fig. 6f, after storage in an air environment with RH  $\sim 20\%$  for 320 h, the 2T tandem cell based on inverted CsPbI<sub>3</sub> PSCs retained 98% of its initial efficiency, demonstrating excellent stability. Therefore, inverted CsPbI<sub>3</sub> PSCs show great potential for application in tandem devices.

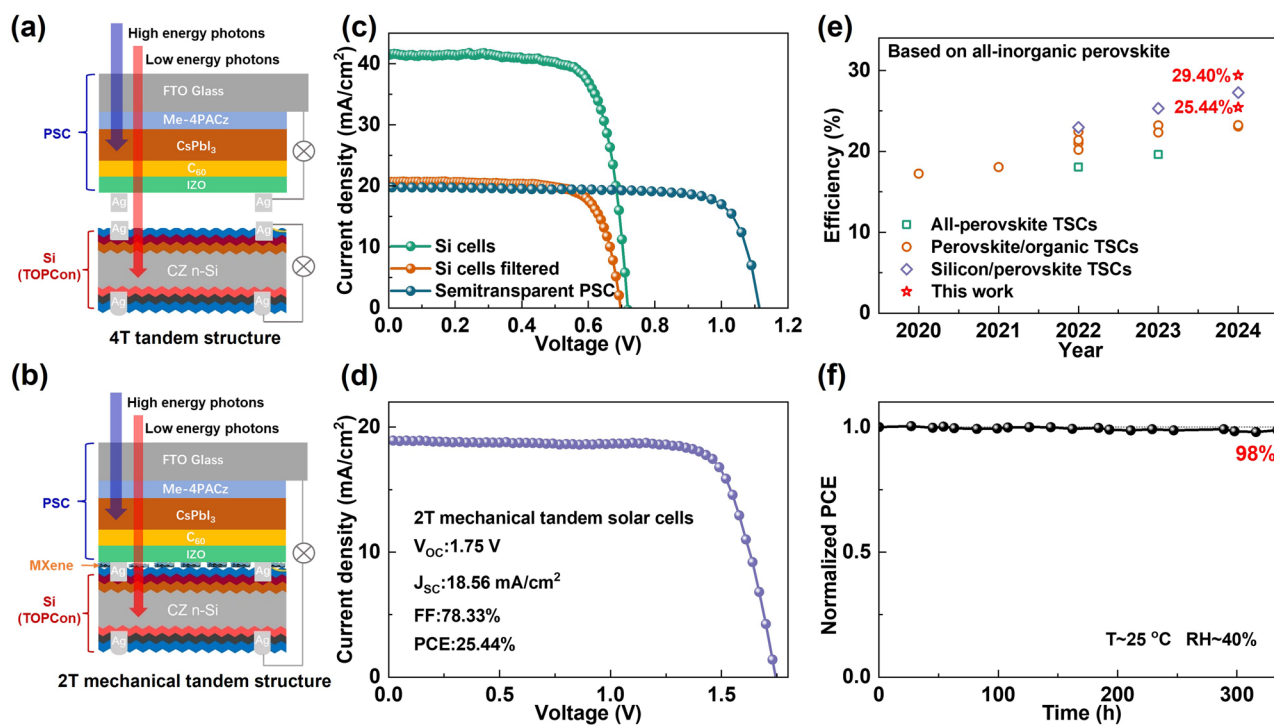


**Fig. 6** Performance and stability of all-inorganic perovskite/silicon tandem devices. **a, b** Schematic diagram of the 4T and 2T mechanically tandem device structure based on the inverted CsPbI<sub>3</sub> PSC and silicon solar cell. **c** *J*-*V* curves of semi-transparent CsPbI<sub>3</sub> PSC, silicon solar cell before and after shading. **d** *J*-*V* curves of the 2T perovskite/silicon mechanically tandem device. **e** Summary of tandem device based on all-inorganic perovskite solar cells. **f** Storage stability of the two-terminal tandem device in an air environment with RH ~40%

## 4 Conclusion

In conclusion, the lanthanide compound TbCl<sub>3</sub> doping was employed to improve the wettability and optoelectronic properties of Me-4PACz, enhancing the crystallization of CsPbI<sub>3</sub> films with large grains and smooth surface. The Tb<sup>3+</sup> and Cl<sup>-</sup> could diffuse into the CsPbI<sub>3</sub> perovskite lattice, enhancing the stability of black phase. Moreover, the excessive Cl<sup>-</sup> passivates the V<sub>1</sub> defects at the buried interface, suppressing non-radiative recombination loss and enhancing the V<sub>OC</sub>. Meanwhile, TbCl<sub>3</sub> improved the energy band alignment between the CsPbI<sub>3</sub> film and Me-4PACz, enhancing the efficiency of the inverted CsPbI<sub>3</sub> PSCs to 18.68% and exhibiting excellent stability. Meantime, the CsPbI<sub>3</sub> PSCs were used to fabricate 4T and 2T perovskite/silicon mechanically tandem devices, achieving efficiencies of 29.40% and 25.44%, respectively. Therefore, this provides a novel method for preparing highly efficient and stable all-inorganic PSCs and perovskite/silicon tandem solar cells, and accelerating the commercialization of PSCs.

**Acknowledgements** The authors gratefully acknowledge the financial support from the National Natural Science Foundation of China (62274132, 62204189, 62274126), the Postdoctoral Fellowship Program of CPSF (GZC20241301), Fundamental Research Funds for the Central Universities (ZYTS25221), and the National Key R&D Program of China (2022YFB3605402, 2021YFF0500501).

**Author Contributions** Wenming Chai contributed to investigation, data curation, and writing—original draft preparation. Weidong Zhu contributed to conceptualization, methodology, writing—reviewing and editing. He Xi contributed to formal analysis. Dazheng Chen contributed to formal analysis. Hang Dong contributed to formal analysis. Long Zhou contributed to formal analysis. Hailong You contributed to supervision. Jincheng Zhang contributed to supervision. Chunfu Zhang contributed to supervision, resources, funding acquisition, writing—reviewing and editing. Chunxiang Zhu contributed to formal analysis. Yue Hao contributed to supervision.

## Declarations

**Conflict of Interest** The authors declare no interest conflict. They have no known competing financial interests or personal relationships that could have appeared to influence the work reported in this paper.

**Open Access** This article is licensed under a Creative Commons Attribution 4.0 International License, which permits use, sharing,

adaptation, distribution and reproduction in any medium or format, as long as you give appropriate credit to the original author(s) and the source, provide a link to the Creative Commons licence, and indicate if changes were made. The images or other third party material in this article are included in the article's Creative Commons licence, unless indicated otherwise in a credit line to the material. If material is not included in the article's Creative Commons licence and your intended use is not permitted by statutory regulation or exceeds the permitted use, you will need to obtain permission directly from the copyright holder. To view a copy of this licence, visit <http://creativecommons.org/licenses/by/4.0/>.

**Supplementary Information** The online version contains supplementary material available at <https://doi.org/10.1007/s40820-025-01763-8>.

## References

1. C. Duan, K. Zhang, Z. Peng, S. Li, F. Zou et al., Durable all-inorganic perovskite tandem photovoltaics. *Nature* **637**(8048), 1111–1117 (2025). <https://doi.org/10.1038/s41586-024-08432-7>
2. X. Chu, Q. Ye, Z. Wang, C. Zhang, F. Ma et al., Surface *in situ* reconstruction of inorganic perovskite films enabling long carrier lifetimes and solar cells with 21% efficiency. *Nat. Energy* **8**(4), 372–380 (2023). <https://doi.org/10.1038/s41560-023-01220-z>
3. F. Sahli, J. Werner, B.A. Kamino, M. Bräuninger, R. Monnard et al., Fully textured monolithic perovskite/silicon tandem solar cells with 25.2% power conversion efficiency. *Nat. Mater.* **17**(9), 820–826 (2018). <https://doi.org/10.1038/s41563-018-0115-4>
4. X. Zhao, T. Liu, Q.C. Burlingame, T. Liu, R. Holley 3rd et al., Accelerated aging of all-inorganic, interface-stabilized perovskite solar cells. *Science* **377**(6603), 307–310 (2022). <https://doi.org/10.1126/science.abn5679>
5. L. Liu, H. Xiao, K. Jin, Z. Xiao, X. Du et al., 4-terminal inorganic perovskite/organic tandem solar cells offer 22% efficiency. *Nano-Micro Lett.* **15**(1), 23 (2022). <https://doi.org/10.1007/s40820-022-00995-2>
6. X. Liu, J. Zhang, H. Wang, Y. Miao, T. Guo et al., CsPbI<sub>3</sub> perovskite solar module with certified aperture area efficiency >18% based on ambient-moisture-assisted surface hydrolysis. *Joule* **8**(10), 2851–2862 (2024). <https://doi.org/10.1016/j.joule.2024.06.026>
7. L. Duan, H. Zhang, M. Liu, M. Grätzel, J. Luo, Phase-pure  $\gamma$ -CsPbI<sub>3</sub> for efficient inorganic perovskite solar cells. *ACS Energy Lett.* **7**(9), 2911–2918 (2022). <https://doi.org/10.1021/acsenergylett.2c01219>
8. Z. Zhang, R. Ji, M. Kroll, Y.J. Hofstetter, X. Jia et al., Efficient thermally evaporated  $\gamma$ -CsPbI<sub>3</sub> perovskite solar cells. *Adv. Energy Mater.* **11**(29), 2100299 (2021). <https://doi.org/10.1002/aenm.202100299>
9. P. Becker, J.A. Márquez, J. Just, A. Al-Ashouri, C. Hages et al., Low temperature synthesis of stable  $\gamma$ -CsPbI<sub>3</sub> perovskite layers for solar cells obtained by high throughput experimentation. *Adv. Energy Mater.* **9**(22), 1900555 (2019). <https://doi.org/10.1002/aenm.201900555>
10. H. Yang, T. Xu, W. Chen, Y. Wu, X. Guo et al., Iodonium initiators: paving the air-free oxidation of spiro-OMeTAD for efficient and stable perovskite solar cells. *Angew. Chem. Int. Ed.* **63**(5), e202316183 (2024). <https://doi.org/10.1002/anie.202316183>
11. T. Zhang, F. Wang, H.-B. Kim, I.-W. Choi, C. Wang et al., Ion-modulated radical doping of spiro-OMeTAD for more efficient and stable perovskite solar cells. *Science* **377**(6605), 495–501 (2022). <https://doi.org/10.1126/science.abo2757>
12. L. Ye, J. Wu, S. Catalán-Gómez, L. Yuan, R. Sun et al., Super-oxide radical derived metal-free spiro-OMeTAD for highly stable perovskite solar cells. *Nat. Commun.* **15**(1), 7889 (2024). <https://doi.org/10.1038/s41467-024-52199-4>
13. X. Lin, D. Cui, X. Luo, C. Zhang, Q. Han et al., Efficiency progress of inverted perovskite solar cells. *Energy Environ. Sci.* **13**(11), 3823–3847 (2020). <https://doi.org/10.1039/d0ee02017f>
14. T. Wu, L.K. Ono, R. Yoshioka, C. Ding, C. Zhang et al., Elimination of light-induced degradation at the nickel oxide-perovskite heterojunction by aprotic Sulfonium layers towards long-term operationally stable inverted perovskite solar cells. *Energy Environ. Sci.* **15**(11), 4612–4624 (2022). <https://doi.org/10.1039/D2EE01801B>
15. G.E. Eperon, G.M. Paternò, R.J. Sutton, A. Zampetti, A.A. Haghighirad et al., Inorganic caesium lead iodide perovskite solar cells. *J. Mater. Chem. A* **3**(39), 19688–19695 (2015). <https://doi.org/10.1039/c5ta06398a>
16. T. Xu, W. Xiang, J. Yang, D.J. Kubicki, W. Tress et al., Interface modification for efficient and stable inverted inorganic perovskite solar cells. *Adv. Mater.* **35**(31), e2303346 (2023). <https://doi.org/10.1002/adma.202303346>
17. Y. Huang, T. Liu, C. Liang, J. Xia, D. Li et al., Towards simplifying the device structure of high-performance perovskite solar cells. *Adv. Funct. Mater.* **30**(28), 2000863 (2020). <https://doi.org/10.1002/adfm.202000863>
18. Z. Zhou, S. Pang, Highly efficient inverted hole-transport-layer-free perovskite solar cells. *J. Mater. Chem. A* **8**(2), 503–512 (2020). <https://doi.org/10.1039/c9ta10694d>
19. J. Wang, J. Zhang, Y. Zhou, H. Liu, Q. Xue et al., Highly efficient all-inorganic perovskite solar cells with suppressed non-radiative recombination by a Lewis base. *Nat. Commun.* **11**(1), 177 (2020). <https://doi.org/10.1038/s41467-019-13909-5>
20. J. Wang, L. Chen, Z. Qian, G. Ren, J. Wu et al., Optimal intermediate adducts regulate low-temperature CsPbI<sub>2</sub>Br crystallization for efficient inverted all-inorganic perovskite solar cells. *J. Mater. Chem. A* **8**(47), 25336–25344 (2020). <https://doi.org/10.1039/D0TA07663E>
21. J. Zhang, J. Long, Z. Huang, J. Yang, X. Li et al., Obstructing interfacial reaction between NiO<sub>x</sub> and perovskite to enable



- efficient and stable inverted perovskite solar cells. *Chem. Eng. J.* **426**, 131357 (2021). <https://doi.org/10.1016/j.cej.2021.131357>
22. Z. Xu, J. Wang, Z. Liu, C. Xiao, J. Wang et al., Self-assembled monolayer suppresses interfacial reaction between NiO<sub>x</sub> and perovskite for efficient and stable inverted inorganic perovskite solar cells. *ACS Appl. Mater. Interfaces* **16**(40), 53811–53821 (2024). <https://doi.org/10.1021/acsami.4c11177>
23. W. Zhao, P. Guo, J. Wu, D. Lin, N. Jia et al., TiO<sub>2</sub> electron transport layer with p-n homojunctions for efficient and stable perovskite solar cells. *Nano-Micro Lett.* **16**(1), 191 (2024). <https://doi.org/10.1007/s40820-024-01407-3>
24. J.J. Yoo, G. Seo, M.R. Chua, T.G. Park, Y. Lu et al., Efficient perovskite solar cells *via* improved carrier management. *Nature* **590**(7847), 587–593 (2021). <https://doi.org/10.1038/s41586-021-03285-w>
25. S.A. Paniagua, A.J. Giordano, O.L. Smith, S. Barlow, H. Li et al., Phosphonic acids for interfacial engineering of transparent conductive oxides. *Chem. Rev.* **116**(12), 7117–7158 (2016). <https://doi.org/10.1021/acs.chemrev.6b00061>
26. X. Zheng, Z. Li, Y. Zhang, M. Chen, T. Liu et al., Co-deposition of hole-selective contact and absorber for improving the processability of perovskite solar cells. *Nat. Energy* **8**(5), 462–472 (2023). <https://doi.org/10.1038/s41560-023-01227-6>
27. D. Xu, M. Wu, Y. Bai, B. Wang, H. Zhou et al., Record-efficiency inverted CsPbI<sub>3</sub> perovskite solar cells enabled by rearrangement and hydrophilic modification of SAMs. *Adv. Funct. Mater.* **35**(2), 2412946 (2025). <https://doi.org/10.1002/adfm.202412946>
28. S.S. Mali, J.V. Patil, S.R. Rondiya, N.Y. Dzade, J.A. Steele et al., Terbium-doped and dual-passivated  $\gamma$ -CsPb(I<sub>1-x</sub>Br<sub>x</sub>)<sub>3</sub> inorganic perovskite solar cells with improved air thermal stability and high efficiency. *Adv. Mater.* **34**(29), e2203204 (2022). <https://doi.org/10.1002/adma.202203204>
29. Y. Wu, L. Lin, Z. Li, Y. Zhang, Z. Feng et al., Temperature sensing of novel Tb<sup>3+</sup>/Ho<sup>3+</sup>/Bi<sup>3+</sup> co-doped lead-free double perovskite Cs<sub>2</sub>AgInCl<sub>6</sub> nanocrystals. *J. Lumin.* **268**, 120430 (2024). <https://doi.org/10.1016/j.jlumin.2023.120430>
30. A. Kulkarni, R. Sarkar, S. Akel, M. Häser, B. Klingebiel et al., A universal strategy of perovskite ink - substrate interaction to overcome the poor wettability of a self-assembled monolayer for reproducible perovskite solar cells. *Adv. Funct. Mater.* **33**(47), 2305812 (2023). <https://doi.org/10.1002/adfm.202305812>
31. A. Sun, C. Tian, R. Zhuang, C. Chen, Y. Zheng et al., High open-circuit voltage (1.197 V) in large-area (1 cm<sup>2</sup>) inverted perovskite solar cell via interface planarization and highly polar self-assembled monolayer. *Adv. Energy Mater.* **14**(8), 2303941 (2024). <https://doi.org/10.1002/aenm.202303941>
32. A. Farag, T. Feeney, I.M. Hossain, F. Schackmar, P. Fassl et al., Evaporated self-assembled monolayer hole transport layers: lossless interfaces in p-i-n perovskite solar cells. *Adv. Energy Mater.* **13**(8), 2203982 (2023). <https://doi.org/10.1002/aenm.202203982>
33. Y. Wang, S. Akel, B. Klingebiel, T. Kirchartz, Hole transporting bilayers for efficient micrometer-thick perovskite solar cells. *Adv. Energy Mater.* **14**(5), 2302614 (2024). <https://doi.org/10.1002/aenm.202302614>
34. Z. Song, W. Xu, Y. Wu, S. Liu, W. Bi et al., Incorporating of lanthanides ions into perovskite film for efficient and stable perovskite solar cells. *Small* **16**(40), e2001770 (2020). <https://doi.org/10.1002/sml.202001770>
35. T. Lyu, P. Dorenbos, Z. Wei, Designing LiTaO<sub>3</sub>: Ln<sup>3+</sup>, Eu<sup>3+</sup> (Ln = Tb or Pr) perovskite dosimeter with excellent charge carrier storage capacity and stability for anti-counterfeiting and flexible X-ray imaging. *Chem. Eng. J.* **461**, 141685 (2023). <https://doi.org/10.1016/j.cej.2023.141685>
36. C. Qiu, X. Lin, Y. Wang, G. Feng, C. Ling et al., Exploring the charge dynamics and energy loss in printable mesoscopic perovskite solar cells. *Adv. Energy Mater.* **12**(47), 2202813 (2022). <https://doi.org/10.1002/aenm.202202813>
37. A. Al-Ashouri, M. Marčinkas, E. Kasparavičius, T. Malinauskas, A. Palmstrom et al., Wettability improvement of a carbazole-based hole-selective monolayer for reproducible perovskite solar cells. *ACS Energy Lett.* **8**(2), 898–900 (2023). <https://doi.org/10.1021/acseenergylett.2c02629>
38. R. Zhuang, L. Wang, J. Qiu, L. Xie, X. Miao et al., Effect of molecular configuration of additives on perovskite crystallization and hot carriers behavior in perovskite solar cells. *Chem. Eng. J.* **463**, 142449 (2023). <https://doi.org/10.1016/j.cej.2023.142449>
39. Q. Ye, F. Ma, Y. Zhao, S. Yu, Z. Chu et al., Stabilizing  $\gamma$ -CsPbI<sub>3</sub> perovskite via phenylethylammonium for efficient solar cells with open-circuit voltage over 1.3 V. *Small* **16**(50), e2005246 (2020). <https://doi.org/10.1002/sml.202005246>
40. Y. Cui, J. Shi, F. Meng, B. Yu, S. Tan et al., A versatile molten-salt induction strategy to achieve efficient CsPbI<sub>3</sub> perovskite solar cells with a high open-circuit voltage. *Adv. Mater.* **34**(45), 2205028 (2022). <https://doi.org/10.1002/adma.202205028>
41. S. Liu, J. Lyu, D. Zhou, X. Zhuang, Z. Shi et al., Dual modification engineering via lanthanide-based halide quantum dots and black phosphorus enabled efficient perovskite solar cells with high open-voltage of 123.5 V. *Adv. Funct. Mater.* **32**(19), 2112647 (2022). <https://doi.org/10.1002/adfm.202112647>
42. F. Liu, Q. Dong, M.K. Wong, A.B. Djurišić, A. Ng, Z. Ren, J. Dai, Is excess PbI<sub>2</sub> beneficial for perovskite solar cell performance? *Adv. Energy Mater.* **6**(7), 1502206 (2016). <https://doi.org/10.1002/aenm.201502206>
43. H. Zhong, X. Liu, M. Liu, S. Yin, Z. Jia et al., Suppressing the crystallographic disorders induced by excess PbI<sub>2</sub> to achieve trade-off between efficiency and stability for PbI<sub>2</sub>-rich perovskite solar cells. *Nano Energy* **105**, 108014 (2023). <https://doi.org/10.1016/j.nanoen.2022.108014>
44. W. Chai, W. Zhu, Z. Zhang, D. Liu, Y. Ni et al., CsPbBr<sub>3</sub> seeds improve crystallization and energy level alignment for highly efficient CsPbI<sub>3</sub> perovskite solar cells. *Chem. Eng. J.* **452**, 139292 (2023). <https://doi.org/10.1016/j.cej.2022.139292>
45. J. Zhang, B. Che, W. Zhao, Y. Fang, R. Han et al., Polar species for effective dielectric regulation to achieve high-performance CsPbI<sub>3</sub> solar cells. *Adv. Mater.* **34**(41), 2202735 (2022). <https://doi.org/10.1002/adma.202202735>

46. H. Wang, Q. Zhang, Z. Lin, H. Liu, X. Wei et al., Spatially selective defect management of CsPbI<sub>3</sub> films for high-performance carbon-based inorganic perovskite solar cells. *Sci. Bull.* **69**(8), 1050–1060 (2024). <https://doi.org/10.1016/j.scib.2024.01.038>
47. S. Wang, T. Sakurai, W.J. Wen, Y.B. Qi, Energy level alignment at interfaces in metal halide perovskite solar cells. *Adv. Mater. Interfaces* **5**(22), 1800260 (2018). <https://doi.org/10.1002/admi.201800260>
48. M. Zhang, Q. Chen, R. Xue, Y. Zhan, C. Wang et al., Reconfiguration of interfacial energy band structure for high-performance inverted structure perovskite solar cells. *Nat. Commun.* **10**(1), 4593 (2019). <https://doi.org/10.1038/s41467-019-12613-8>
49. Z. Saki, K. Aitola, K. Sveinbjörnsson, W. Yang, S. Svanström et al., The synergistic effect of dimethyl sulfoxide vapor treatment and C<sub>60</sub> electron transporting layer towards enhancing current collection in mixed-ion inverted perovskite solar cells. *J. Power. Sources* **405**, 70–79 (2018). <https://doi.org/10.1016/j.jpowsour.2018.09.100>
50. X. Deng, D. Zhang, Y. Chen, S. Yang, characteristic mode analysis: application to electromagnetic radiation, scattering, and coupling problems. *Chin. J. Electron.* **32**(4), 663–677 (2023). <https://doi.org/10.23919/cje.2022.00.200>
51. Y. Chen, J. Wu, S. Zhang, X. Zhu, B. Zou et al., Effective energy transfer boosts emission of rare-earth double perovskites: the bridge role of Sb(III) doping. *J. Phys. Chem. Lett.* **14**(31), 7108–7117 (2023). <https://doi.org/10.1021/acs.jpclt.3c01825>
52. R.J. Sutton, G.E. Eperon, L. Miranda, E.S. Parrott, B.A. Kamino, J.B. Patel, H.J. Snaith, Bandgap-tunable cesium lead halide perovskites with high thermal stability for efficient solar cells. *Adv. Energy Mater.* **6**(8), 1502458 (2016). <https://doi.org/10.1002/aenm.201502458>
53. J. Tian, Q. Xue, X. Tang, Y. Chen, N. Li et al., Dual interfacial design for efficient CsPbI<sub>2</sub>Br perovskite solar cells with improved photostability. *Adv. Mater.* **31**(23), 1901152 (2019). <https://doi.org/10.1002/adma.201901152>
54. H. Wang, M. Yang, W. Cai, Z. Zang, Suppressing phase segregation in CsPbI<sub>2</sub>Br<sub>2</sub> films via anchoring halide ions toward underwater solar cells. *Nano Lett.* **23**(10), 4479–4486 (2023). <https://doi.org/10.1021/acs.nanolett.3c00815>
55. H. Choi, J. Jeong, H.-B. Kim, S. Kim, B. Walker et al., Cesium-doped methylammonium lead iodide perovskite light absorber for hybrid solar cells. *Nano Energy* **7**, 80–85 (2014). <https://doi.org/10.1016/j.nanoen.2014.04.017>
56. M.B. Faheem, B. Khan, C. Feng, M.U. Farooq, F. Raziq et al., All-inorganic perovskite solar cells: energetics, key challenges, and strategies toward commercialization. *ACS Energy Lett.* **5**(1), 290–320 (2020). <https://doi.org/10.1021/acsenergylett.9b02338>
57. H. Li, W. Zhang, Perovskite tandem solar cells: from fundamentals to commercial deployment. *Chem. Rev.* **120**(18), 9835–9950 (2020). <https://doi.org/10.1021/acs.chemrev.9b00780>
58. T. Han, W. Zhu, T. Wang, M. Yang, Y. Zhou et al., MXene-interconnected two-terminal, mechanically-stacked perovskite/silicon tandem solar cell with high efficiency. *Adv. Funct. Mater.* **34**(12), 2311679 (2024). <https://doi.org/10.1002/adfm.202311679>
59. X. Lian, Y. Shi, X. Shen, X. Wan, Z. Cai et al., Design of high performance MXene/oxide structure memristors for image recognition applications. *Chin. J. Electron.* **33**(2), 336–345 (2024). <https://doi.org/10.23919/cje.2022.00.125>

**Publisher's Note** Springer Nature remains neutral with regard to jurisdictional claims in published maps and institutional affiliations.

